



This is a repository copy of *Microstructural evolution and wear mechanism of Ti₃AlC₂ – Ti₂AlC dual MAX phase composite consolidated by spark plasma sintering (SPS)*.

White Rose Research Online URL for this paper:
<https://eprints.whiterose.ac.uk/150380/>

Version: Accepted Version

Article:

Magnus, C., Cooper, D., Sharp, J. et al. (1 more author) (2019) Microstructural evolution and wear mechanism of Ti₃AlC₂ – Ti₂AlC dual MAX phase composite consolidated by spark plasma sintering (SPS). *Wear*, 438-439. 203013. ISSN 0043-1648

<https://doi.org/10.1016/j.wear.2019.203013>

Article available under the terms of the CC-BY-NC-ND licence
(<https://creativecommons.org/licenses/by-nc-nd/4.0/>).

Reuse

This article is distributed under the terms of the Creative Commons Attribution-NonCommercial-NoDerivs (CC BY-NC-ND) licence. This licence only allows you to download this work and share it with others as long as you credit the authors, but you can't change the article in any way or use it commercially. More information and the full terms of the licence here: <https://creativecommons.org/licenses/>

Takedown

If you consider content in White Rose Research Online to be in breach of UK law, please notify us by emailing eprints@whiterose.ac.uk including the URL of the record and the reason for the withdrawal request.



eprints@whiterose.ac.uk
<https://eprints.whiterose.ac.uk/>

Microstructural evolution and wear mechanism of $\text{Ti}_3\text{AlC}_2\text{-Ti}_2\text{AlC}$ dual MAX-phase composite consolidated by spark plasma sintering (SPS)

Carl Magnus^{1*}, Daniel Cooper^{1,2}, Joanne Sharp¹, and William M. Rainforth¹

¹ Department of Materials Science and Engineering, University of Sheffield, Sir Robert Hadfield Building, Mappin St, Sheffield, S1 3JD, UK.

² Seaborg Technologies, Titangade 11, 2200 Copenhagen, Denmark.

Keywords: MAX phases; Deformation; Frictional heating; Wear mechanism; Grain buckling

Abstract

In this work, we report the synthesis, deformation and tribological behaviour of a novel $\text{Ti}_3\text{AlC}_2\text{-Ti}_2\text{AlC}$ MAX phase composite metallo-ceramic. The dual MAX phase composite was synthesized by spark plasma sintering under vacuum environment using Ti, Al, and C precursor powders. The deformation mechanism and the tribological behaviour were studied and analyzed by SEM, TEM, and Raman spectroscopy. The transition in friction and wear as well as the operative wear mechanisms involved were further discussed. Detailed analysis of the worn surface showed that the $\text{Ti}_3\text{AlC}_2\text{-Ti}_2\text{AlC}$ MAX phase composite is intrinsically self-lubricating.

1. Introduction

The nanolaminates known as the $\text{M}_{n+1}\text{AX}_n$ phases (MAX-phases), are highly anisotropic hexagonal layered ternary machineable carbides and nitrides, where M represents an early transitional metal, A is a group A element (mostly from group 13 and 14), and X is either C and/or N [1]. According to their n-values, the hexagonal crystal structure crystallizing in $\text{P6}_3/\text{mmc}$ space group can be further categorized as “211-phase” for M_2AX ($n=1$), “312-phase” for M_3AX_2 ($n=2$) and “413-phase” for M_4AX_3 ($n=3$), etc [2, 3]. The major difference between the crystal structures of these phases is the number of M-layers separating the A-layers. In the “211 phase” there are two, in the “312 phase” three, whilst in the “413 phase” there are four [4]. This class of materials combines some attractive properties of ceramics and metals simultaneously to endow them with unusual and exceptional electrical, thermal, elastic, chemical and mechanical properties [5, 6]. The chemical bonding in MAX phases is anisotropic and metallic-covalent-ionic in nature [7], whilst the metallic and covalent contribution plays a significant role [8]. Mechanically, however, they represent the only class of polycrystalline

solids that deform by a range of energy absorbing mechanisms such as grain buckling, kink band formation and delamination of individual grains which in turns renders them extremely damage tolerant [2, 5, 9, 10]. Some important properties of this family of metallo-ceramics are high melting point, damage tolerance at room temperature, high thermal and electrical conductivity, good high-temperature-oxidation resistance and machinability [7].

Ti_2AlC and Ti_3AlC_2 are both layered ceramics belonging to a series generated from the MAX-phase family $Ti_{n+1}AlC_n$ ($n = 1 - 2$). Fig. 1 shows the crystal structures of Ti_3AlC_2 and Ti_2AlC with atomic configuration in the unit cells. Previous work [11-13] have shown that it is difficult to synthesize monolithic phase Ti_2AlC or Ti_3AlC_2 , as in most cases the fabrication of either of these phases has always led to the formation of the other alongside as an ancillary phase due to the reaction mechanisms. It is also common to have TiC coexisting with these phases during synthesis; this has however been linked to the reaction mechanism, possible decomposition at high sintering temperature as well as the synthesis method [11, 14-16]. Thus the reaction mechanism(s) can be exploited to aid the fabrication of a 100 % layered composite.

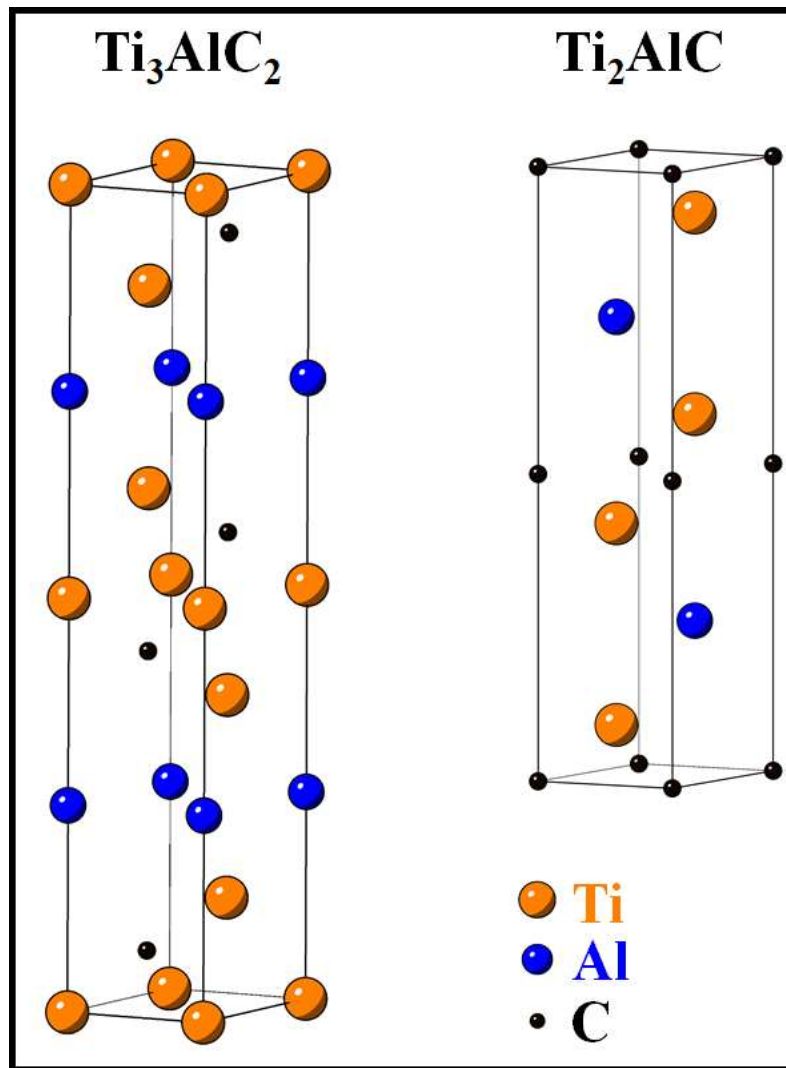


Fig. 1. Crystal structures of Ti_3AlC_2 and Ti_2AlC with atomic configuration in the unit cells.

The purpose of this work is to attempt to fabricate a dual MAX phase Ti_3AlC_2 - Ti_2AlC composite via elemental powder route using spark plasma sintering (SPS) and characterize the resulting layered composite microstructural evolution as well as its deformation microstructure upon indentation. This work further aims to evaluate the friction and wear behaviour of this unique layered microstructure via detailed analysis of the worn surface chemically and microstructurally in order to elucidate the underlining wear mechanism(s). It is important to note that owing to the mismatch in coefficient of thermal expansion (CTE) between Ti_2AlC ($8.2 \times 10^{-6} K^{-1}$) and Ti_3AlC_2 ($9.0 \times 10^{-6} K^{-1}$) although small [17, 18], might be enough to trigger some shrinkage cracking that might severe the mechanical properties of this composite system.

2. Experimental procedure

2.1. Materials and methods

Commercially available Ti (titanium metal), Al (aluminium metal) and C (graphite) precursor powders were used as starting materials. The powder characteristics of these as-received powders are presented in Table 1. The powder mixture was mixed in a planetary ball mill according to the molar ratio described in Table 1 and then poured in a 20 mm graphite die. The graphite die was then placed in a spark plasma sintering (SPS) furnace (Fig. 2) and sintered at 1100 °C for 8 min with a pressure of 30 MPa under vacuum. The sample was heated at a rate 50 °C/min with surface temperature continuously monitored with the aid of an infrared pyrometer.

Table 1. Powder characteristics and precursor formulation

Powder	Supplier	Purity (%)	Particle size	Starting powder (g)	Comments
Ti	Aldrich	99.7	-100 mesh	5.17	All powders were milled together in one step for 10 min
Al	Acros Organics	99	-200 mesh	1.68	
C	Fischer-Chemicals	General purpose grade	n/a	0.65	

**Milled powder was then subsequently SPSed*

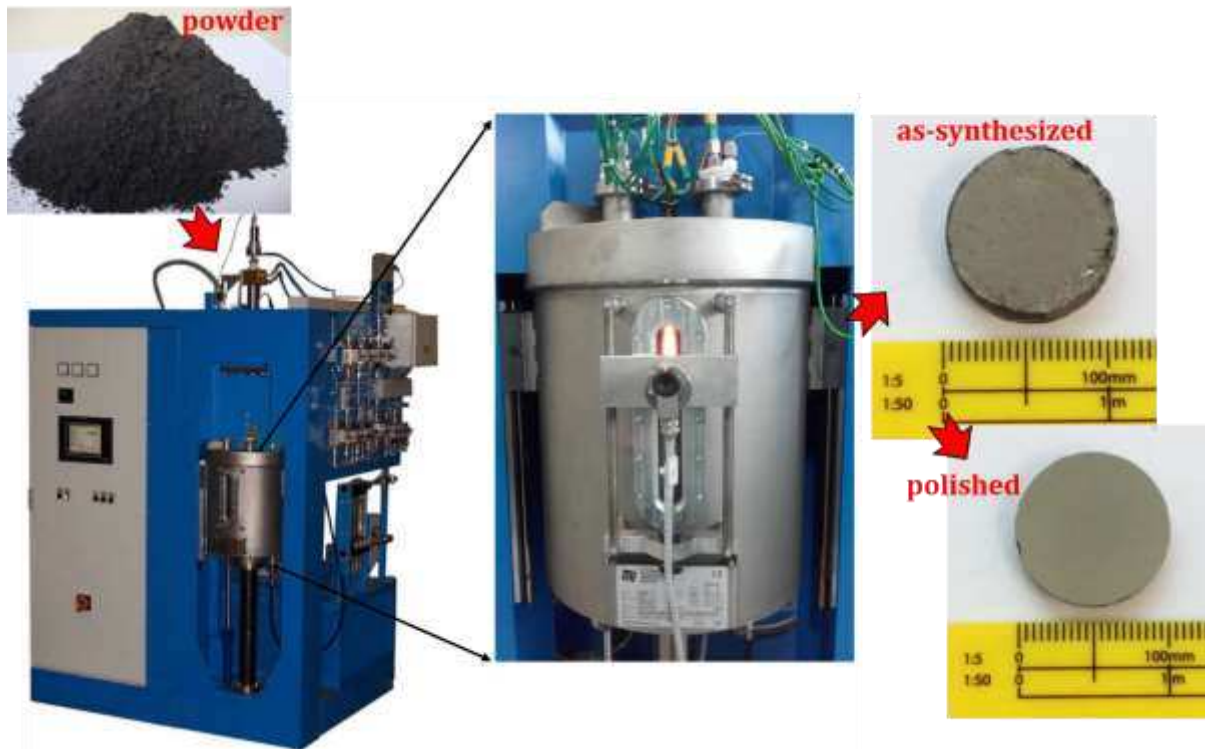


Fig. 2. HPD 25 spark plasma sintering (SPS) set-up and resulting cylindrical bulk samples.

2.2. Analytical methodology

Phase composition of the sintered sample was investigated using X-ray diffraction (D2 PHASER, BRUKER, USA) and phase fractions determined using the Rietveld refinement method. The microstructure was analyzed with SEM (FEI Inspect F50, The Netherlands) equipped with an EDS detector (Oxford Instruments, AZtec), TEM (JEOL 2010F operating at 200 kV (JEOL Ltd, Japan); Philips EM420 operating at 120 kV) and Raman spectroscopy ex situ by employing a Si-calibrated Raman spectrometer (inVia Renishaw Co., UK) with a He-Ne laser (wavelength of 532 nm, laser output power 20 mW). Focused ion beam (FIB) instrument (FEI Helios NanoLab G3 UC, FEI company, Netherlands) was used to prepare samples for cross-sectional transmission electron microscopy with Pt layer deposited to protect the area of interest.

The density of the sintered sample was measured using Archimedes method with distilled water used as the immersion medium and relative density calculated by taking into consideration the theoretical density of Ti_3AlC_2 (4.25g/cm^3) [14] and Ti_2AlC (4.11g/cm^3) [19]. Hardness testing was carried out using Vickers micro indentation (DuraScan G5, emco TEST) using a 4.9 N load with a dwell time of 15 sec. Five readings were taken at different locations which were then averaged to get the final hardness value. The deformation microstructures upon contact damage by indentation was observed using optical microscopy and scanning electron microscopy.

Friction and wear tribological testing was conducted in a pin-on-disk rotary tribometer (CETR, UMT-1), using a 4 mm-diameter Al_2O_3 ball counterpart in ambient air dry sliding condition. The rotational speed was 50 rpm, and the normal load was 0.5 N producing a wear track length of ~ 7 mm. The wear track were measured by employing a surface profilometer (Veeco, Dektak 150) and specific wear rates calculated using the equation:

$$K = V/L \times N$$

Where K, V, L, and N represents specific wear rate, volume, sliding distance and load, respectively. Wear volume (V) was calculated by determining cross-sectional area of the wear track and multiplying by the wear track length. Worn surfaces were characterized by scanning electron microscopy and the chemistry of the tribofilm evaluated using Raman spectroscopy as well as quantitatively analyzed using electron energy loss spectroscopy (TEM/EELS).

3. Results and discussion

3.1. XRD patterns and phase fraction

Fig. 3 shows the characteristic XRD pattern of the resulting dual MAX phase composite after SPS. It can be seen that two phases, Ti_3AlC_2 and Ti_2AlC were the only phases present. More importantly, no presence of TiC was observed in the sintered sample, which implies that all TiC intermediary phase was consumed during the synthesis. Rietveld refinement confirmed that Ti_3AlC_2 is the main crystalline phase with weight fraction 68 % whilst 32 % of the residual phase was Ti_2AlC thus 100 % MAX phase composite was formed.

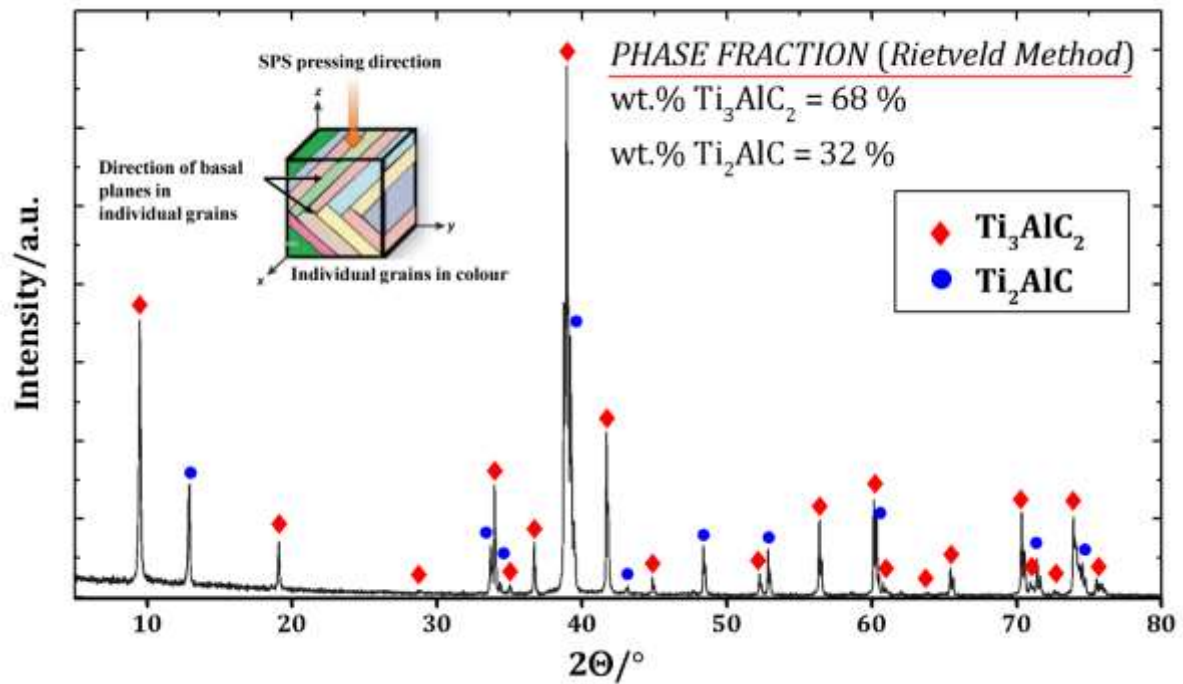


Fig. 3. XRD patterns of the resulting MAX phase composite obtained by in-situ SPS of elemental Ti, Al and C powder mixture.

3.2. Microstructure characterization

SEM micrographs of the polished unetched surface of the in situ-SPSed Ti_3AlC_2 - Ti_2AlC MAX phase composite is shown in Fig. 4. It is interesting that no Al_3Ti intermetallic phase coexists with the MAX phase composite as previous carried out at this sintering temperature led to the formation of Al_3Ti and later disappeared at sintering temperatures above 1200 °C [20]. The micrograph depicts the characteristic layered nature of MAX phases. The microstructure conforms well with the relative density measurement as there is no evidence of porosity indicating complete densification.

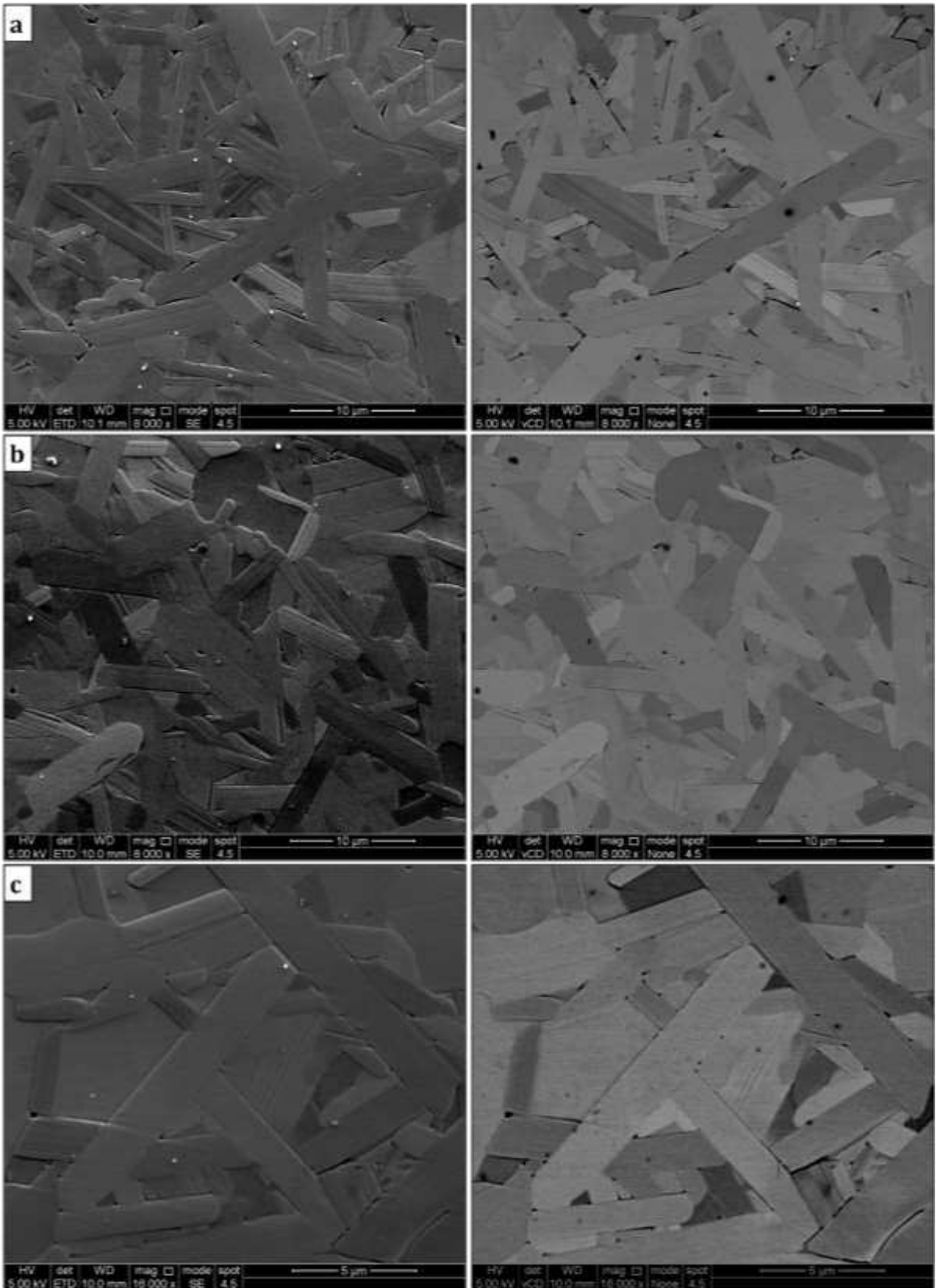


Fig. 4. SEM micrographs of the polished unetched Ti_3AlC_2 - Ti_2AlC MAX phase composite obtained by in situ SPS.

Further analysis by SEM-EDS to identify the phases was undertaken as shown in Fig. 5. Based on the intensity of the peaks, it is clear that the bright phase is the Ti_3AlC_2 phase whilst the dark phase is the Ti_2AlC phase. Phase identification was necessary as it helps to understand the deformation behaviour of these MAX phases.

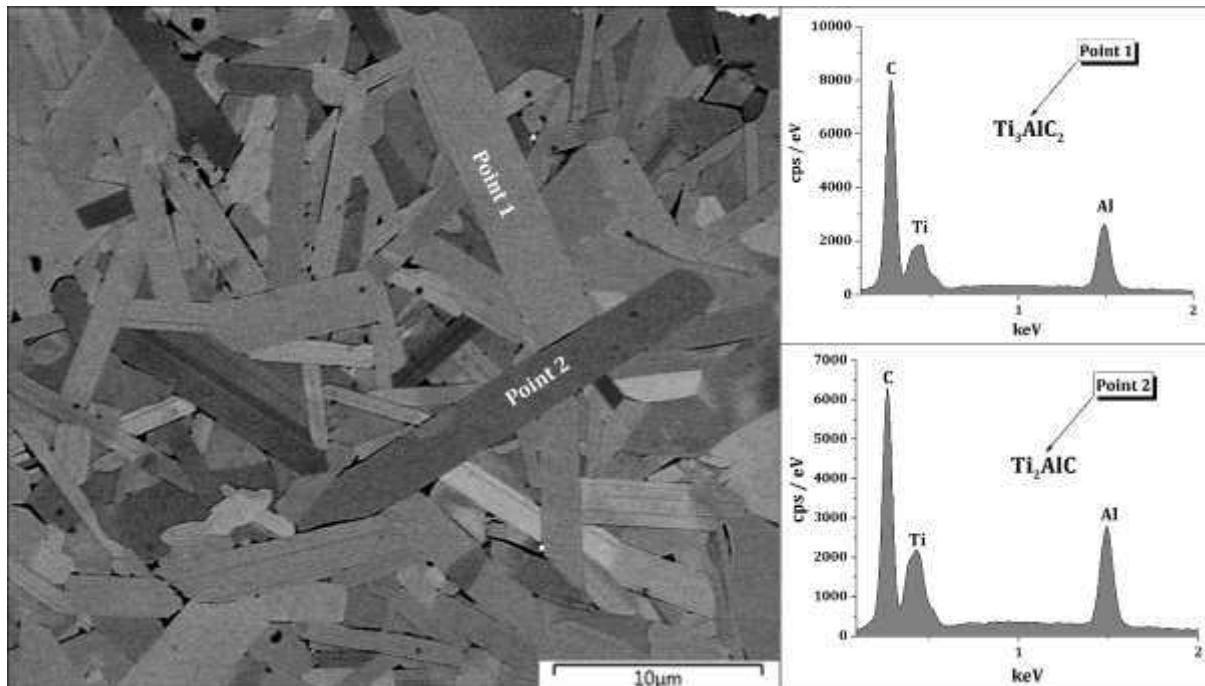


Fig. 5. EDS point spectrum collected from the different phase contrast point 1 and point 2.

Abnormal grain growth (AGG) of the Ti_3AlC_2 and Ti_2AlC grains were observed in some area in the matrix (Fig. 6). The implication of this is not fully understood at this time but such abnormal grain growth have been reported to be detrimental to hardness and fracture toughness due to crack nucleation [21].

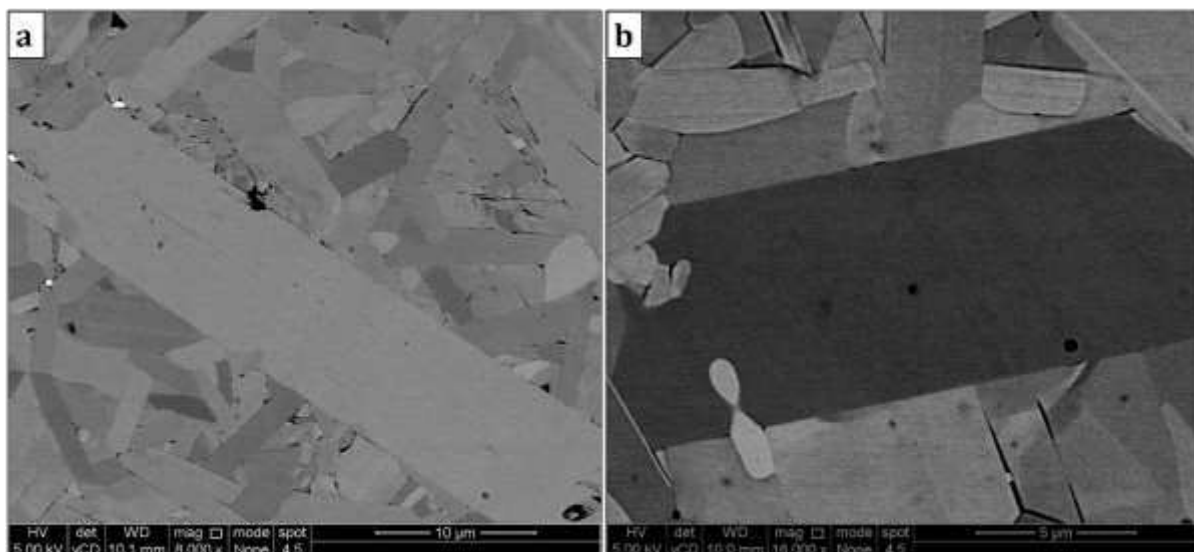


Fig. 6. Abnormal grain growth (AGG) of (a) Ti_3AlC_2 and (b) Ti_2AlC grains in the Ti_3AlC_2 - Ti_2AlC composite matrix.

A detrimental contribution of the abnormal grain growth is the role it plays in gaps and cracking as observed in this composite system (Fig. 7). Since the thermal expansion coefficient (TEC) of Ti_3AlC_2 is higher than that of Ti_2AlC , compressive stress will be imposed on Ti_2AlC , and a tangential tensile stress in Ti_3AlC_2 . During cooling from the requisite sintering temperature of the composite, spontaneous radial microcracking would initiate if the dimension of the Ti_2AlC exceeds the critical size based on the Selsing's model [22]. It is conceivable to attribute the cracking observed in this composite system to thermal expansion coefficient mismatch as well as the abnormal grain growth. The majority of the cracks observed present themselves in the form of gaps along the grain boundary as the boundaries between the grains are the weakest point. In some cases cracks were deflected along the grains upon meeting a plate shape grain.

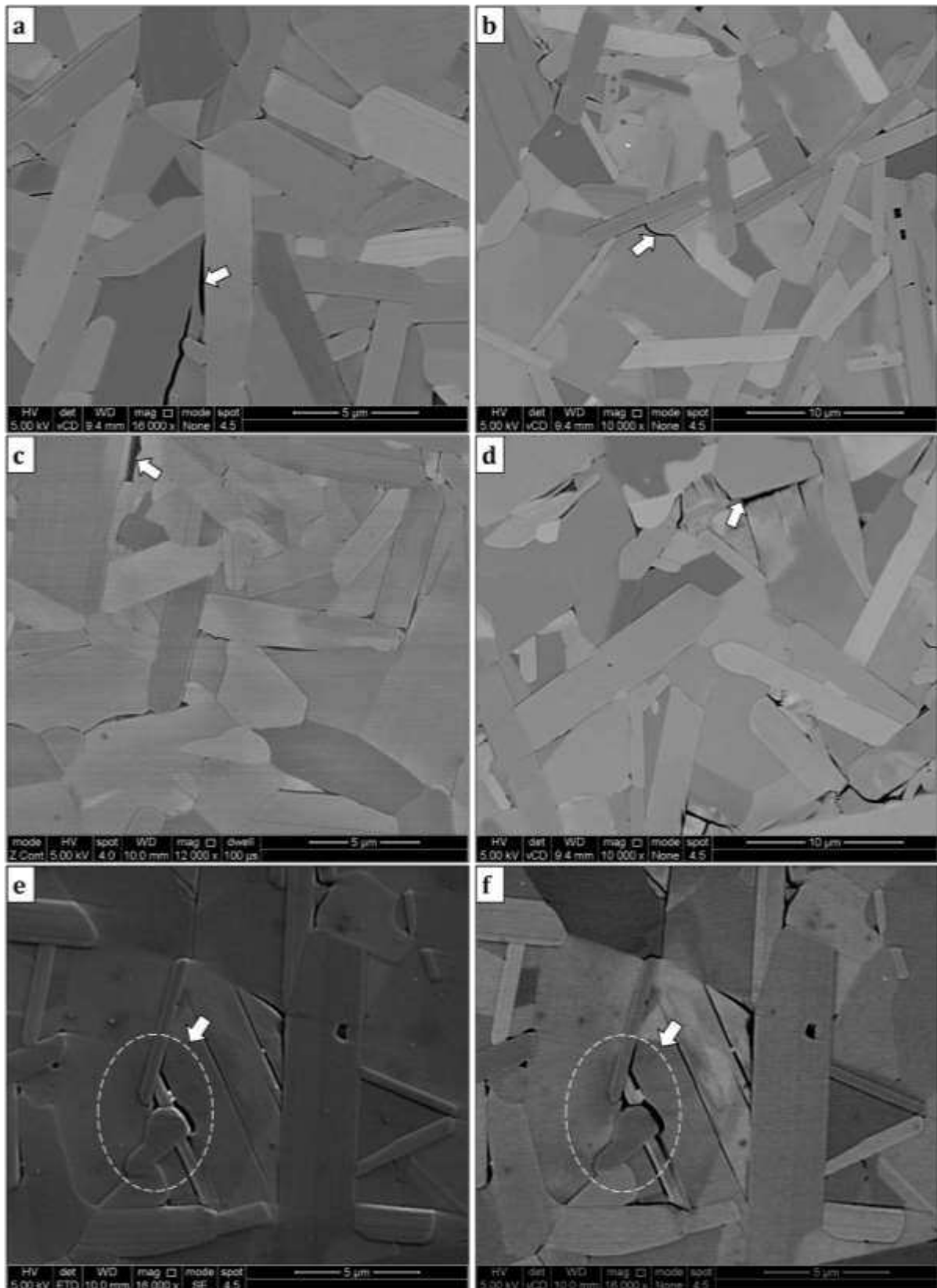


Fig. 7. A collections of SEM micrographs showing gaps and/or microcracking along the grains and grain boundaries.

Other synthesis route discussed in the literature such as hot pressing (HP) as an example have often led to intergrown structures such as $\text{Ti}_3\text{AlC}_2\text{-TiC-Ti}_2\text{AlC}$ [23], $\text{Ti}_3\text{AlC}_2\text{-TiAl}$ [24], and $\text{Ti}_3\text{AlC}_2\text{-TiAl-Ti}_2\text{AlC}$ [25]. These composite structures may possess superior flexural strength as well as minimizing spontaneous microcracking as the binary phase will segregate preferentially along the grain boundary thus creating a pinning effect on the grain growth of the Ti_3AlC_2 and Ti_2AlC grains as reported elsewhere [16].

The characteristic lamellar plate-like TEM microstructure of the polycrystalline $\text{Ti}_3\text{AlC}_2\text{-Ti}_2\text{AlC}$ MAX phase composite is shown in Fig. 8. The grains are essentially planar defect free with no dislocations and/or stacking faults observed in the as-synthesized composite. Both the Ti_3AlC_2 and Ti_2AlC grains are formed of two distinct laminated slab layers (Fig. 8(a)). Fig. 8(b) shows the selected area electron diffraction pattern (SAED) obtained from the different layers (layer 1 and layer 2) in the composite.

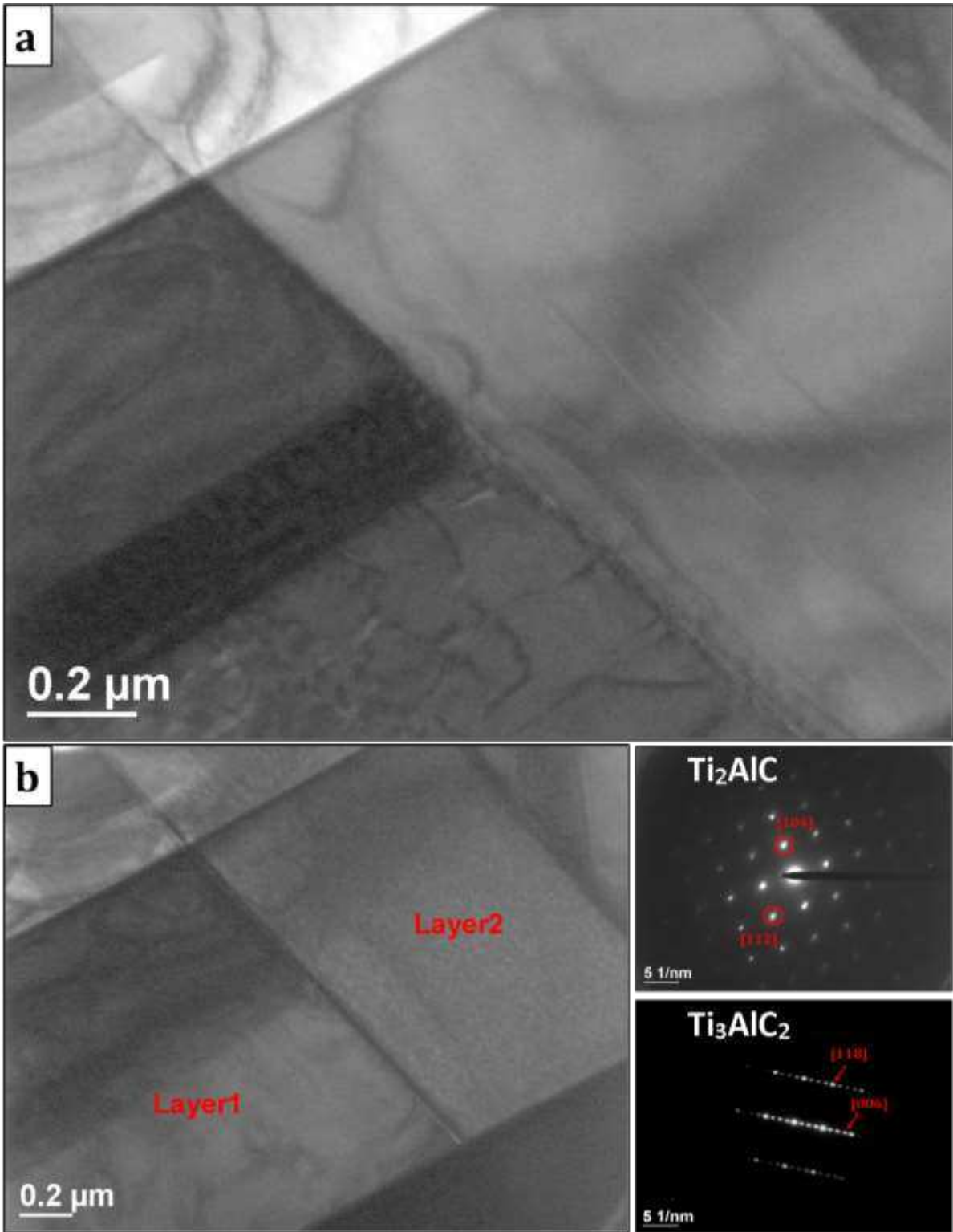


Fig. 8. TEM bright-field (BF) images showing: (a) Ti_3AlC_2 - Ti_2AlC layers and (b) Ti_3AlC_2 - Ti_2AlC layers as well as corresponding selected area diffraction (SAD) pattern (c) layer 1 (Ti_2AlC) and (d) layer 2 (Ti_3AlC_2).

3.3. Density and Vickers hardness

Table 2 is a summary of some of the mechanical properties of TiAl_3 , Ti_3AlC_2 , and Ti_2AlC for comparison. It is of interest to include the properties of TiAl_3 a possible intermetallic phase which often crystallizes from the decomposition of Ti_3AlC_2 and have been found enhance the flexural strength and hardness of Ti_3AlC_2 and Ti_2AlC [16, 24].

The density of the Ti_3AlC_2 - Ti_2AlC bulk composite fabricated by SPS was 4.16 g/cm^3 , which is $\sim 99 \%$ of the combined theoretical value upon considering the phase fraction and theoretical density of Ti_3AlC_2 and Ti_2AlC . This indicates that a dual Ti_3AlC_2 - Ti_2AlC MAX phase composite can be synthesized by SPS at relatively low temperature for short dwell times with high purity and good densification in contrast to other sintering techniques such as hot pressing (HP) where intermediate phases still exist at low temperatures owing to incomplete densification as reported elsewhere [16, 25]. The Vickers microhardness was measured as $\sim 2.9 \text{ GPa}$, which is in the range of the intrinsic hardness of monolithic phase MAX phases reported to be in the range of $2 - 8 \text{ GPa}$ [5] but lower than that of Ti_3AlC_2 (3.5 GPa [26]) and Ti_2AlC (4.5 GPa [17]). It is however not surprising that the Vickers hardness of the composite was lower than of both Ti_3AlC_2 and Ti_2AlC as the presence of voids as shown in Fig. 7 will bring about decreasing hardness and flexural strength as reported elsewhere [16].

Table 2. Comparison of some mechanical properties of TiAl_3 , Ti_3AlC_2 and Ti_2AlC

Properties	TiAl_3	Ti_3AlC_2	Ti_2AlC
Density (g/cm^3)	3.3	4.2	4.1
Vickers hardness (GPa)	6	3.5	4.5
Flexural strength (MPa)	162	375	384
Fracture toughness ($\text{MPa}\cdot\text{m}^{1/2}$)	2	7.2	5.37
Sources	[27]	[26]	[28]

Contact damage by Vickers indentation (Fig. 8 and 9) revealed extensive energy absorbing mechanisms such as grain pull-out, delamination of laminated grains, crack deflection, grain buckling, grain pull-out and push-out in agreement with the damage mechanism observed in Ti_3SiC_2 [10, 29-33]. The optical micrographs (Fig. 8) confirm the evidence of indentation damage with grain pull-out and push-out clearly seen alongside with extensive grain pile-ups. No evidence of indentation cracks emanating from the indentation diagonals was observed as damage appeared to be contained, in consistent with other MAX phases [9, 17, 34].

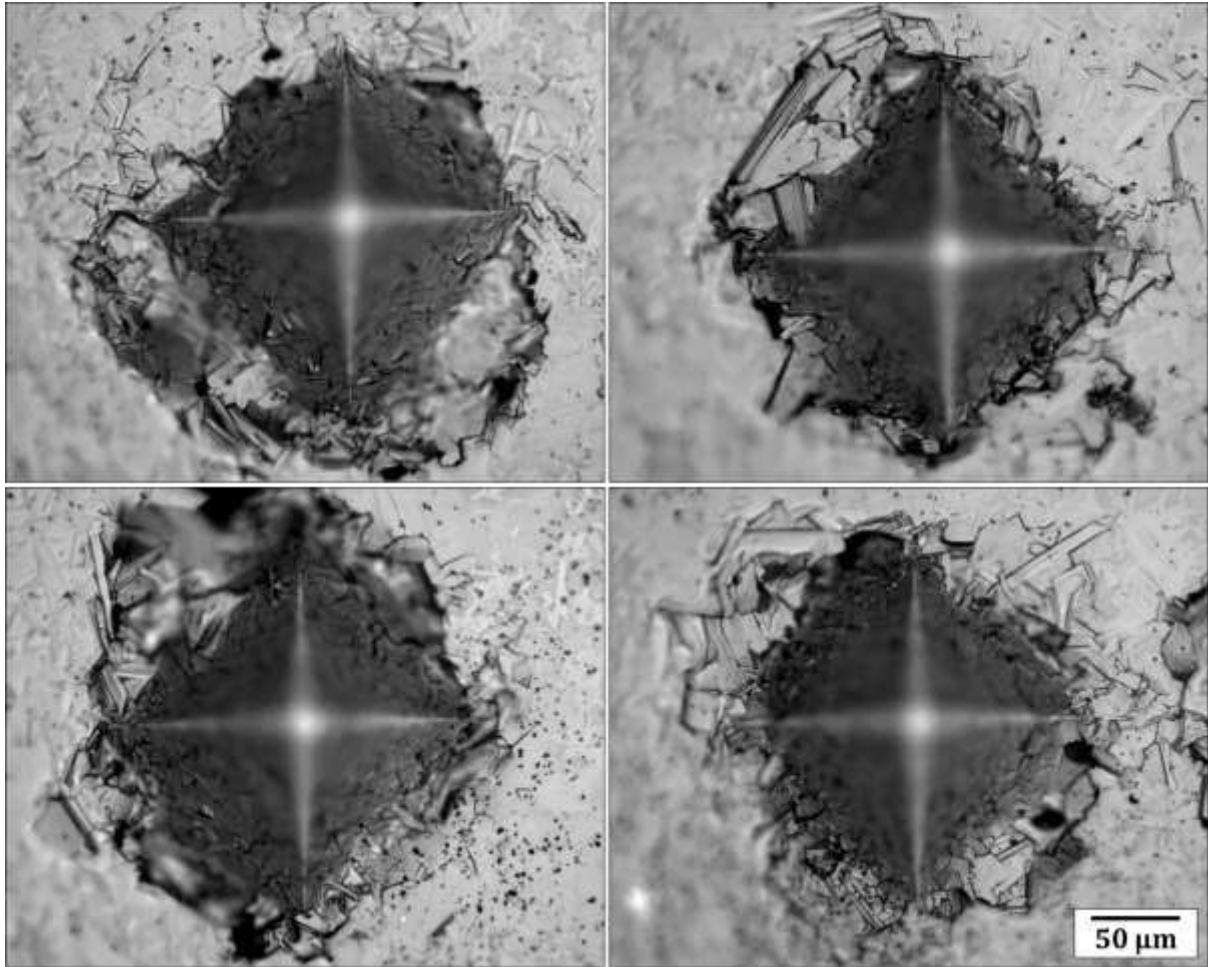


Fig. 8. Optical micrographs showing Vickers indentation damage around the indents. Note the absence of indentation crack from the corners of the indents as well as pile-ups around indent.

In order to obtain a deeper picture of the damage resistance of the $\text{Ti}_3\text{AlC}_2\text{-Ti}_2\text{AlC}$ composite, the indents created by the Vickers indenter were further examined by SEM (Fig. 9). A range of deformation modes such as grain pile-ups (Fig. 9(a)), chevron fold (Fig. 9(b)), delamination and kink-band formation (Fig. 9(c-d)) can be observed upon indentation. This suggests that plastic deformation might be enabled by shear sliding in this composite system.

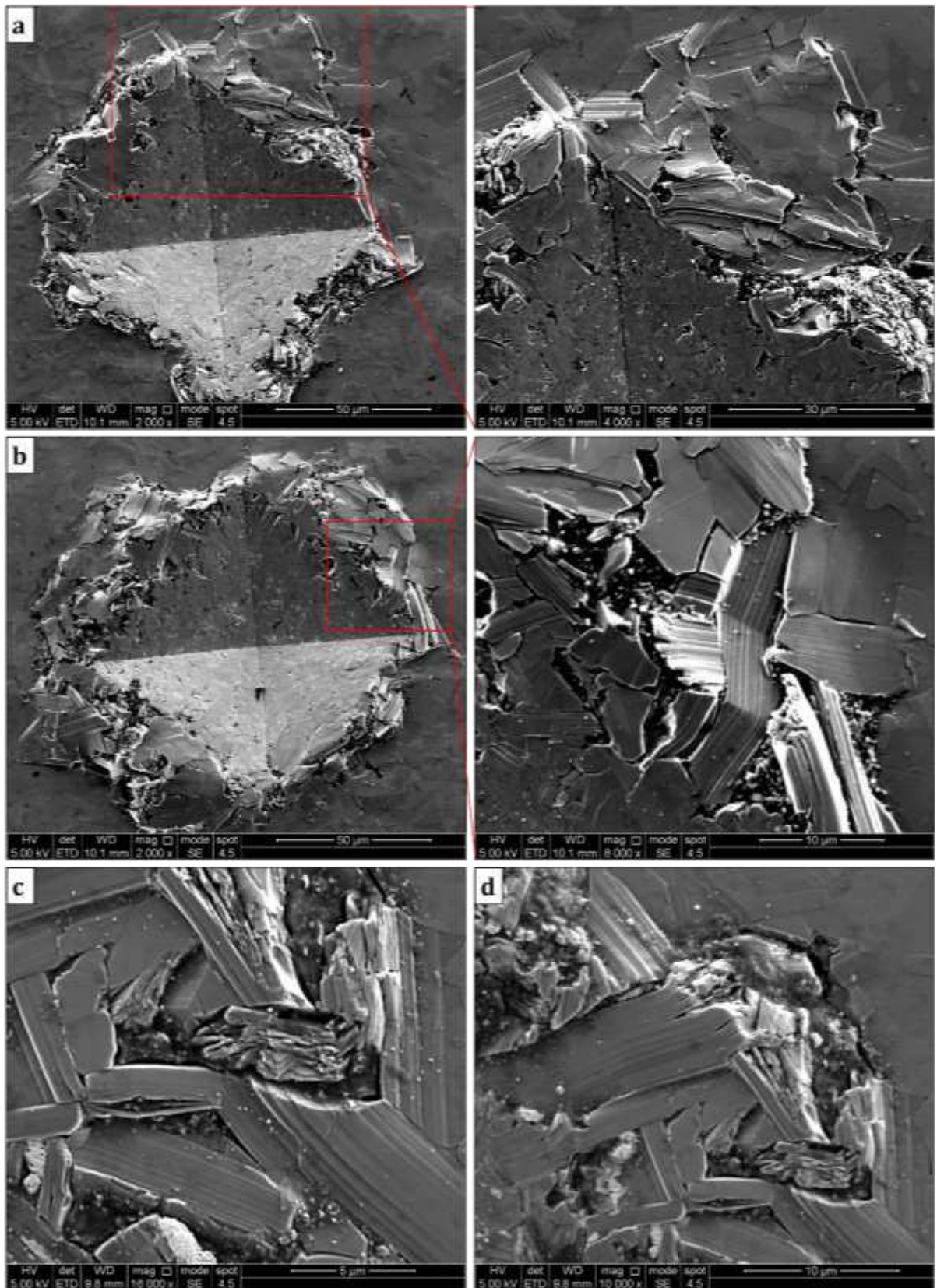


Fig. 9. Scanning electron micrographs (SEM) of the Vickers indentation patterns created on $\text{Ti}_3\text{AlC}_2\text{-Ti}_2\text{AlC}$ MAX phase composite.

Furthermore, the indentation damage zone was further characterized by using a 3D –image analysis software (MountainsMap® SEM Topo, Digital Surf, France) to reconstruct the backscatter SEM image using stereo pairs. Further energy absorbing mechanisms (Fig. 10) not readily seen in the optical micrograph such as grain buckling, grain delamination, kink band formation and grain boundary cracking can be clearly seen. This damage tolerance observed is a hallmark of the MAX phases and has been attributed to basal slip activation as reported elsewhere [35, 36]. Thus in practical applications, the importance of this high-damage tolerance phenomenon i.e., ability of this material to confine damage to small area around indentations cannot be overemphasized.

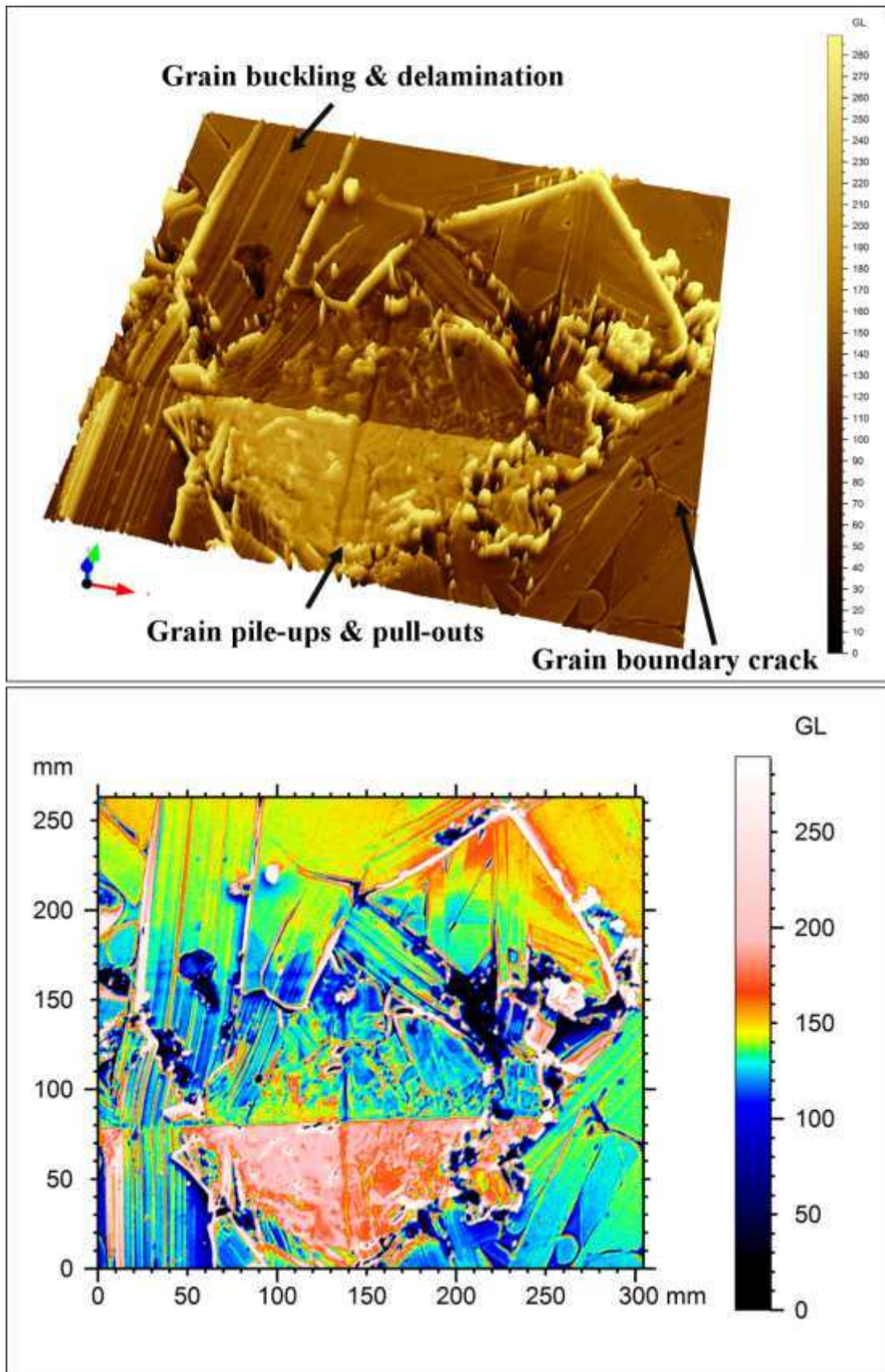


Fig. 10. 3D reconstruction of scanning electron micrograph showing Vickers-induced damage in Ti_3AlC_2 - Ti_2AlC dual MAX phase composite. Note: GL is a depth function.

3.4. Friction coefficient and wear characteristics

The variation of friction coefficient as a function of time under dry sliding conditions at room temperature is shown in Fig. 11. As can be seen, the friction curve exhibits a typical break-in curve as described by Blau [37]. The initial coefficient of friction was high and around ~ 0.75 and attained a steady state around ~ 0.85 when all sharpest asperities are worn off and surface becomes smoother. However, at about 2500 cycles, a transition in friction occurs which further led to a drop in friction coefficient to about ~ 0.35 . The reason for this is not fully understood but one major reason might be attributed to the evolution of oxide films that have grown over time thus becoming tenacious and protective.

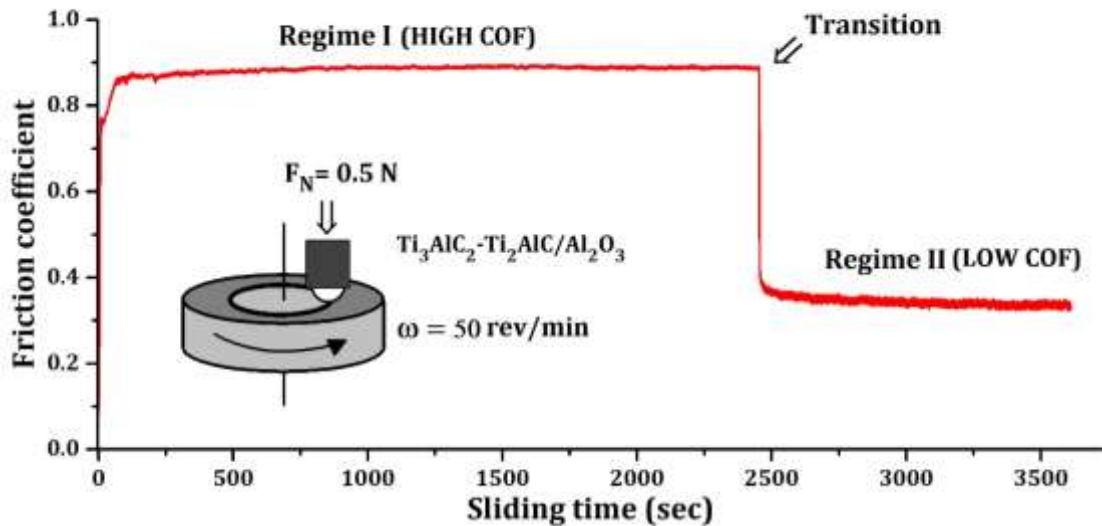


Fig. 11. Dependence of the coefficient of friction as a function of sliding distance.

The measured specific wear rate of the composite was of the order of $10^{-4} \text{ mm}^3(\text{N.m})^{-1}$ which is somewhat lower in comparison with that recorded for Ti_3SiC_2 sliding against steel which was of the order $10^{-3} \text{ mm}^3(\text{N.m})^{-1}$ [38].

3.5. Wear track characterization

3.5.1. Raman analysis

The Raman spectrum obtained from the pristine surface of $\text{Ti}_3\text{AlC}_2\text{-Ti}_2\text{AlC}$ composite and wear track of the $\text{Ti}_3\text{AlC}_2\text{-Ti}_2\text{AlC/Al}_2\text{O}_3$ tribocouple is shown in Figs. 12 and 13. The spectrum recorded shows peaks corresponding solely to Ti_3AlC_2 and Ti_2AlC [39, 40] for the pristine sample whilst titanium oxide (TiO_2) [41, 42], titanium oxycarbide (TiO_xC_y) [43], as well as vibrational modes originating from graphitic carbon [44] were recorded from the wear track.

The presence of TiO_2 shows that the surface temperature during dry sliding increased in the range $500 - 900\text{ }^\circ\text{C}$, the formation temperature range of anatase and possible anatase to rutile transformation [45, 46]. The formation mechanism resulting in the evolution of TiC_xO_y is not fully understood; however its evolution is consistent with results reported elsewhere, and thought to be due to self-generating triboreaction [47, 48]. The D and G graphitic carbon signatures in the wear track on the other hand may be due to the outward diffusion of Ti and Si during dry sliding owing to frictional heating and subsequent reaction with inward diffusion of oxygen to form TiO_2 and SiO_2 respectively leaving behind graphite which possess poor affinity to oxygen [46]. The weak covalent interaction between the Ti and Si layers as well as the layered structure of Ti_3SiC_2 grains enhances the diffusion [46]. However, Raman analysis did not reveal the coexistence of SiO_2 in the tribofilm architecture.

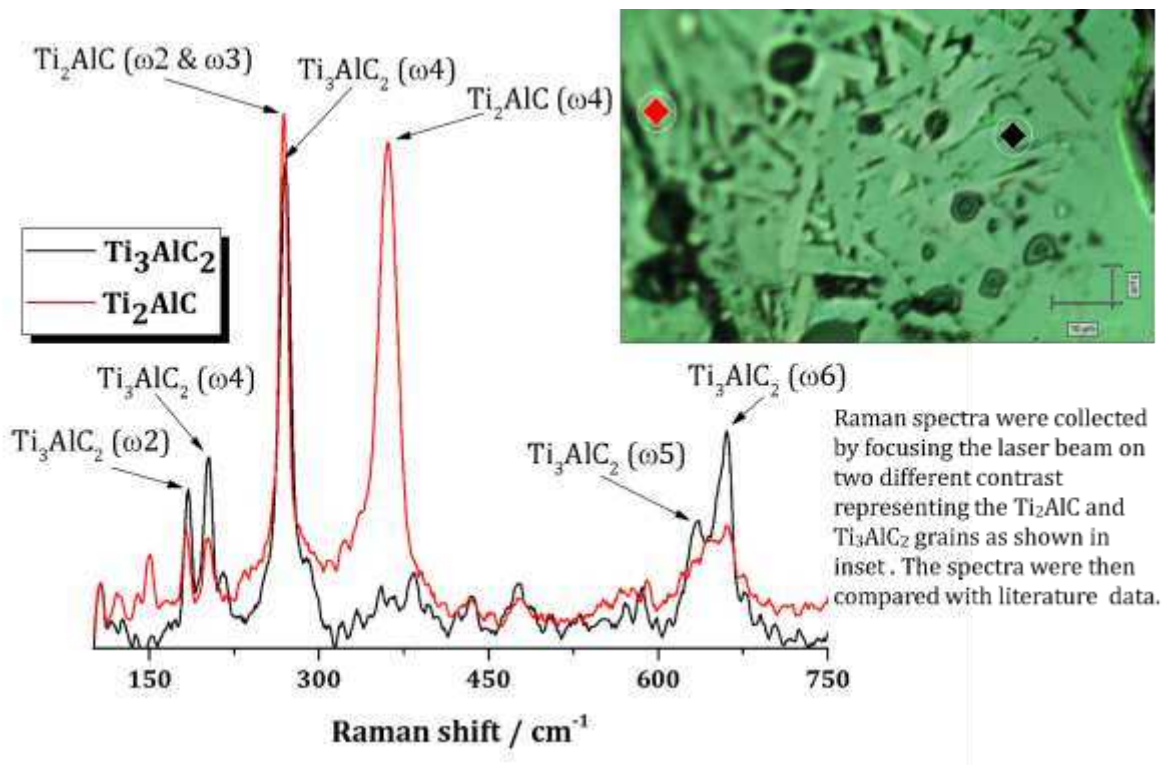


Fig. 12. Raman spectra collected from the polished as-synthesized Ti_3AlC_2 - Ti_2AlC composite.

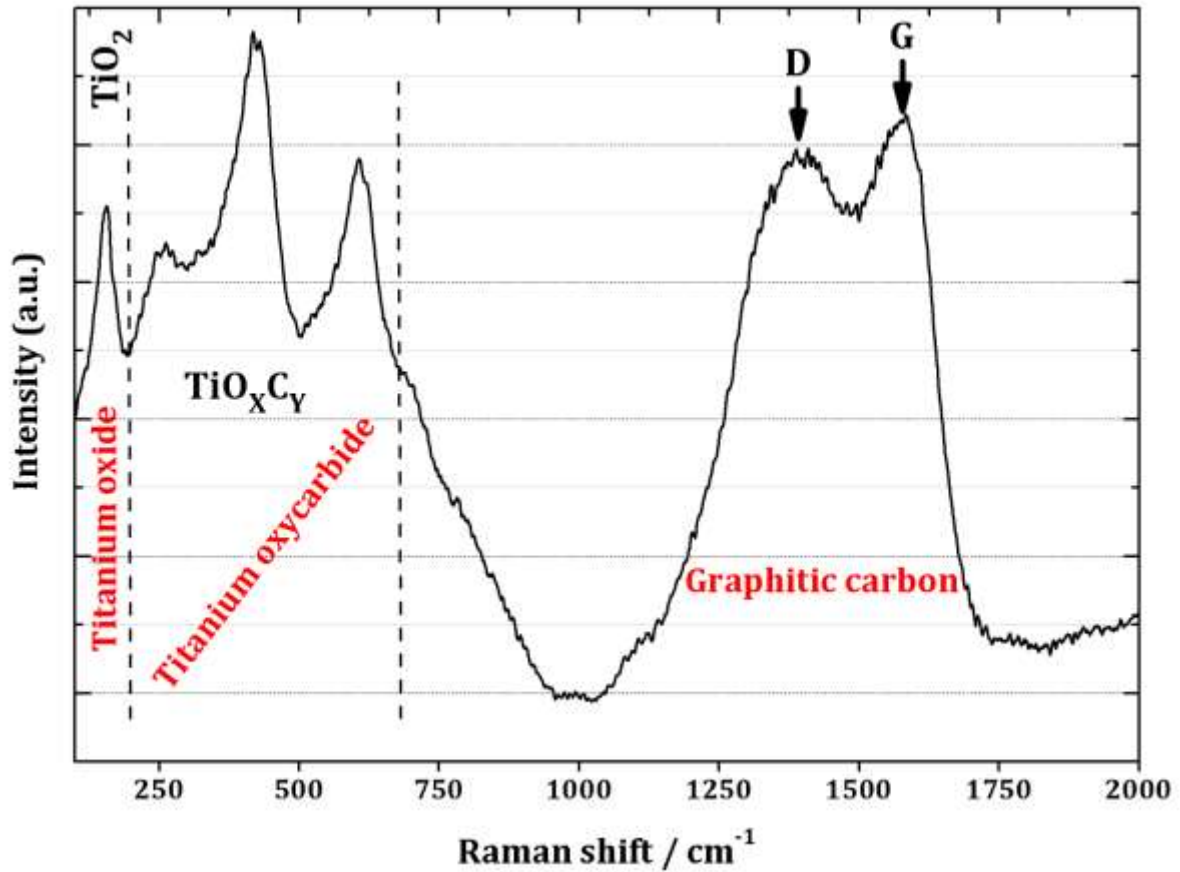


Fig. 13. Raman spectra of an area inside the wear track of Ti_3AlC_2 - Ti_2AlC / Al_2O_3 tribocouple.

3.5.2. Scanning electron microscopy

Fig. 14 show the scanning electron microscopy (SEM) micrographs of the wear track after dry sliding. Some of the grains appeared to have fractured (Fig. 14(a-b)), pulverized and subsequently compacted inside the wear track alongside some loose wear debris distributed inside the wear track. Tribofilms are visible inside the wear track as patches (arrows in Fig. 14(e-f)) and mixed with the compacted wear debris (Fig. 14(e-f)). The grains appear to have been deformed with extensive grain delamination and kink-bands evident inside the wear track (Fig. 14(c-d)). The observed deformation mechanism after dry sliding is consistent with that observed by indentation induced deformation as shown in Fig. 9.

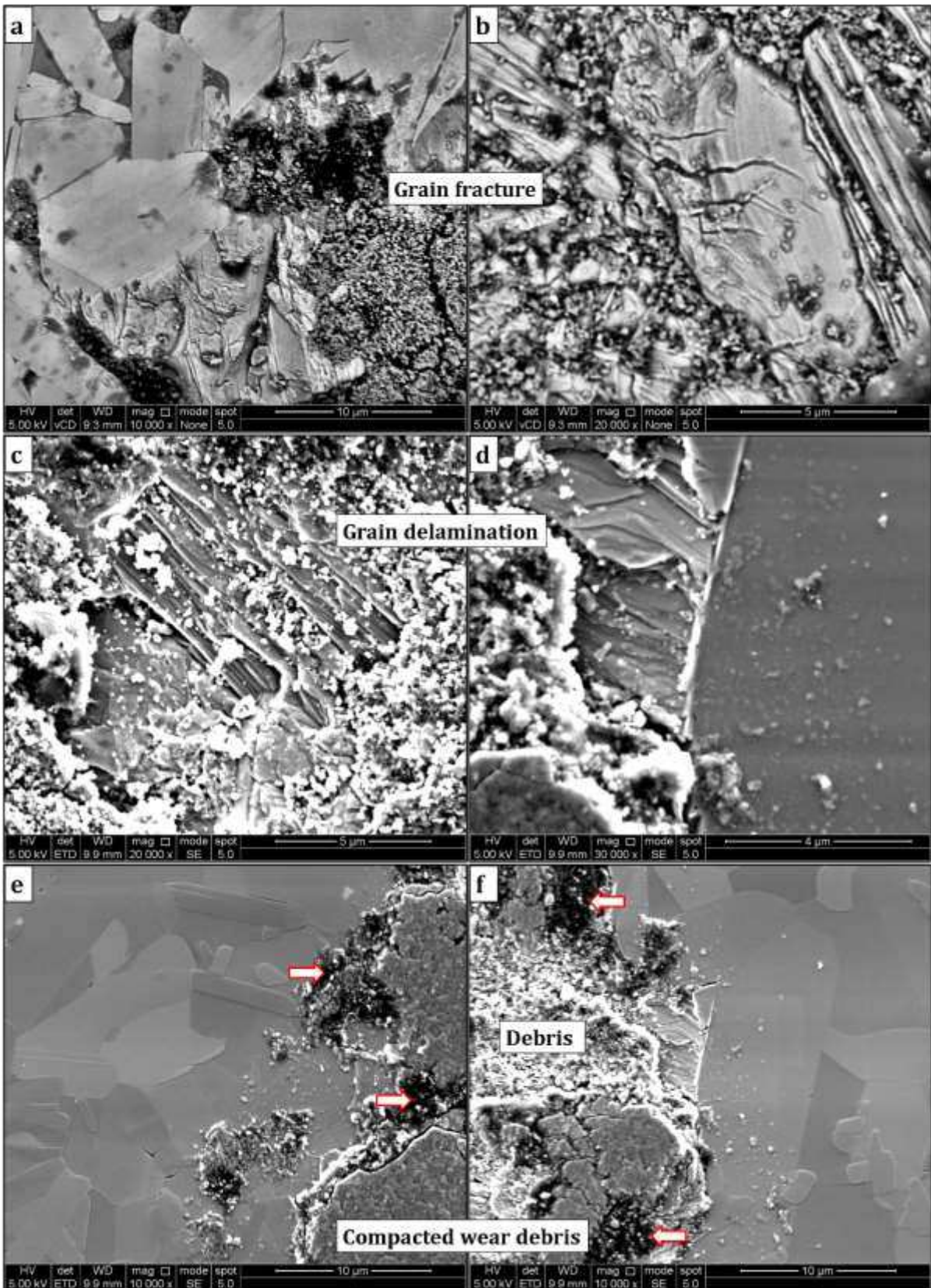


Fig. 14. Shows the BSE-SEM micrographs of the worn surface and associated morphologies of $Ti_3AlC_2-Ti_2AlC$ composite upon dry sliding. Note: arrows in (e-f) shows tribofilms.

3.5.2.1. EDS-analysis

EDS elemental map was collected from the wear track (Fig. 15) to understand the elemental distribution and further compare the results with the Raman analysis. As observed, the arrows as identified in (Fig. 14(e-f)) corresponded essentially to graphite. Whilst the compacted wear debris were heavily oxidized possible due to friction heating that have led to the evolution of TiO_2 and TiO_xC_y on the compacted wear debris surface to further create a lubricious layer.

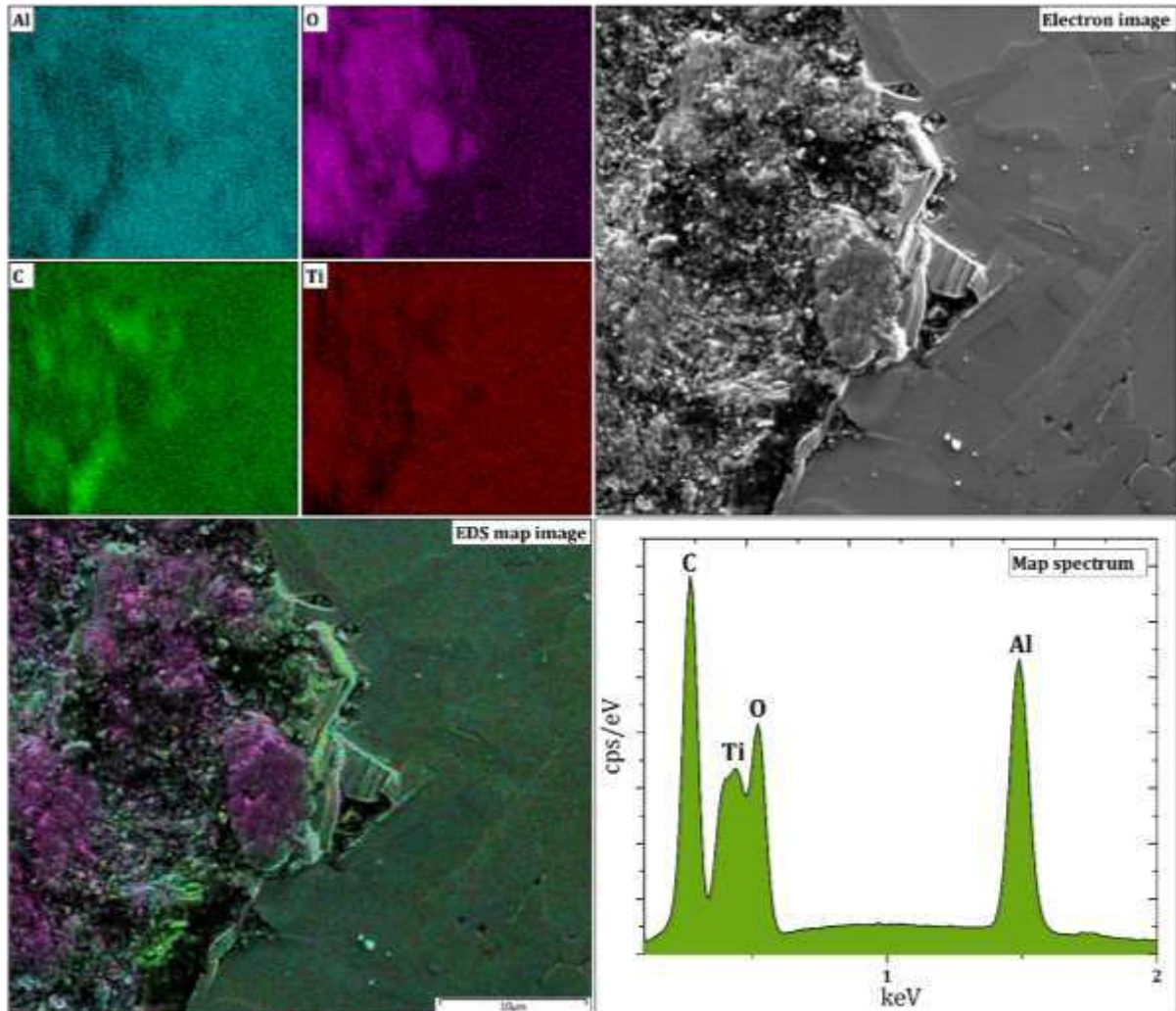


Fig. 15. EDS elemental map taken from the wear track of $\text{Ti}_3\text{AlC}_2\text{-Ti}_2\text{AlC}$ after dry sliding against Al_2O_3 at room temperature.

3.5.3. Transmission electron microscopy

Fig. 16 shows STEM imaging of the FIB lifted-out section and the associated deformed grain as well as EELS elemental mapping analyses of the tribofilm formed on the worn surface after dry sliding at room temperature. The grains appear to have buckled with grain cracking evident along the grain boundary and intergranularly (as shown in Figure 16(a) and highlighted at higher magnification). The worn surface microstructural observation(s) is consistent with that

reported elsewhere [31]. Since the grain boundaries are relatively weak it will thus facilitate nucleation of intergranular cracks [31]. According to [49], the grain buckling of nanolayers within the grains serves as a precursor for the evolution cavities as well as of kink bands. EELS analysis (Fig. 16(b)) of the tribofilm and/or wear debris mixed tribofilm section (from Fig. 16(a)) revealed strong C-K, Ti-L_{2,3}, and O-K edges suggesting coexistence of titanium, oxygen and carbon in the form of titanium oxycarbide consistent with Raman analysis (Fig. 13).

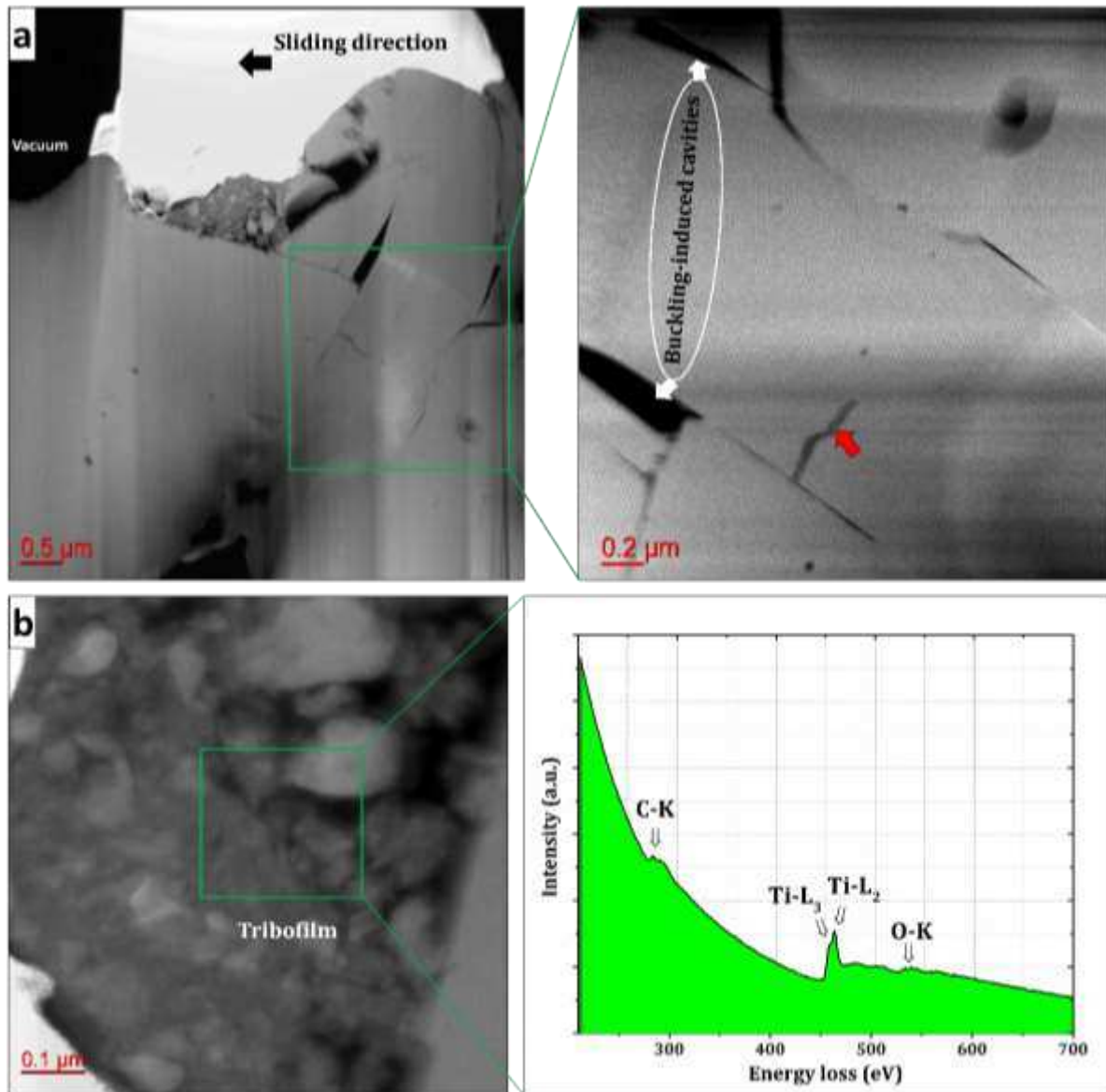


Fig. 16. Cross-sectional HAADF-STEM images inside Ti_3AlC_2 - Ti_2AlC wear surface showing sliding induced deformation (a) and higher magnification of highlighted section, and (b) EELS chemical evolution of the tribolayer.

Bright-field TEM observation of the sliding surface (Fig. 17) revealed that in addition to grain fracture and buckling, some stacking faults exist in response to the sliding deformation.

The reason behind stacking faults is not fully understood at this time but their evolution might be linked to missing atomic planes owing to lattice rotation triggered by kink-band formation and dislocation walls as reported elsewhere [29].

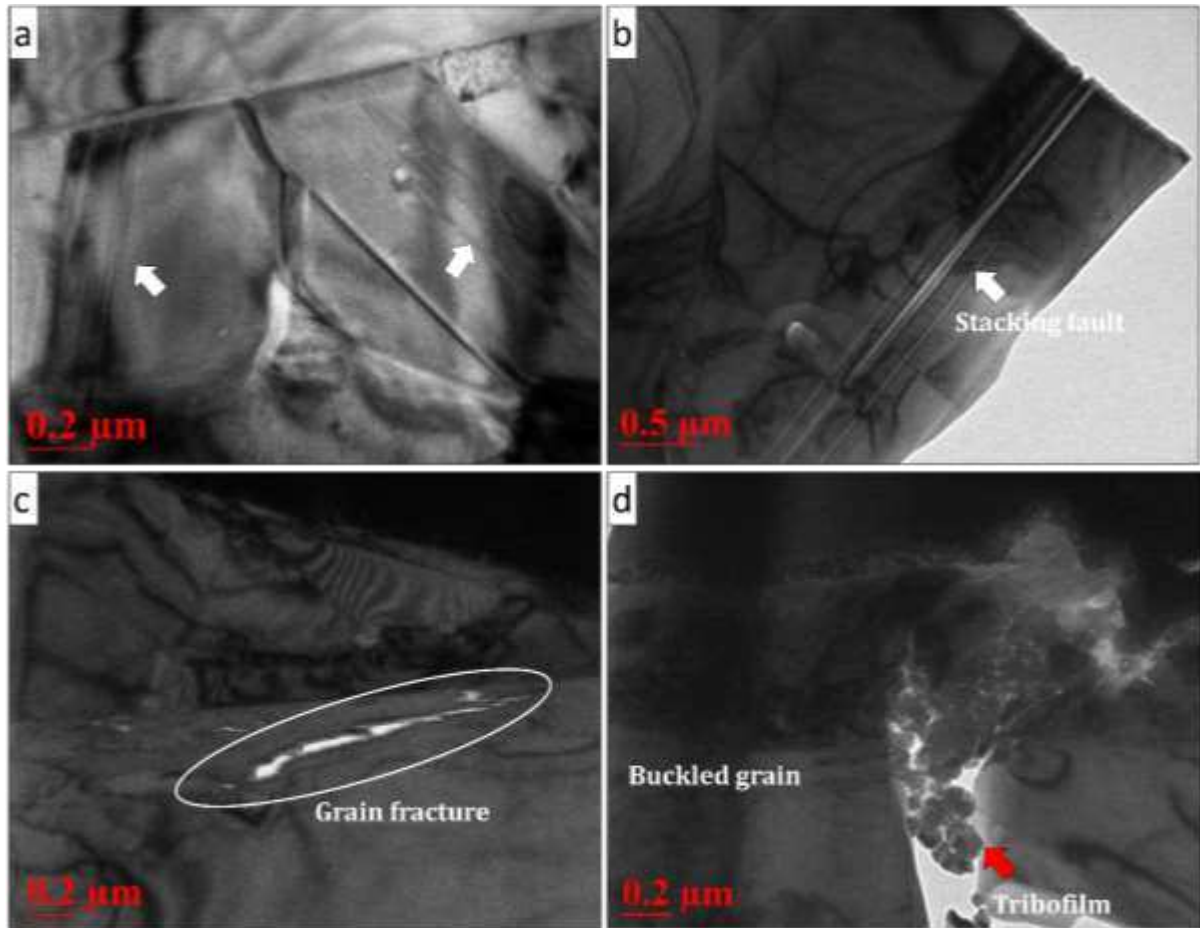


Fig. 17. HAADF-STEM images of wear deformation morphology (a) and (b) high magnification of highlighted section in (a) of the worn surface of Ti_3AlC_2 - Ti_2AlC/Al_2O_3 tribocouple. Note grain boundary cracking in (b) possibly due to dislocation pile-up along the grain boundary.

Bright-field conventional TEM (Fig.18) further shows that dislocations multiplied and arranged themselves in the form of dislocations walls and dislocation debris as a response to grain buckling following extensive deformation. No kink bands were observed other than delamination. This is possibly due to the fact that grain buckling due to sliding deformation did not lead to extensive damage or the FIBed section did not cover the whole deformation mechanisms.

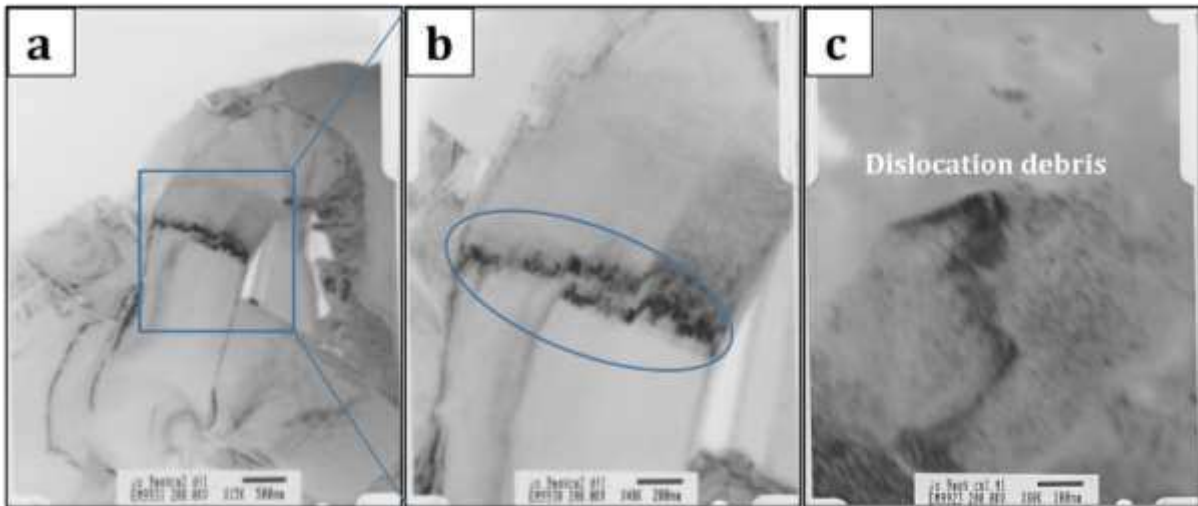


Fig. 18. Bright-field conventional TEM images showing: (a-b) deformed grain with dislocation walls, (b) enlarged region of square outlined in (a) with blue highlights showing dislocation wall and (c) dislocation debris from the worn surface.

4. Alumina ball analysis

Analysis of the alumina ball on upon dry sliding against the composite showed evidence of material transfer to the ball (Fig. 19). Optical images showed possible tribofilm as well as oxidized wear debris on the balls surface. The ball also appeared to have been scratched slightly (Fig. 19(d)).

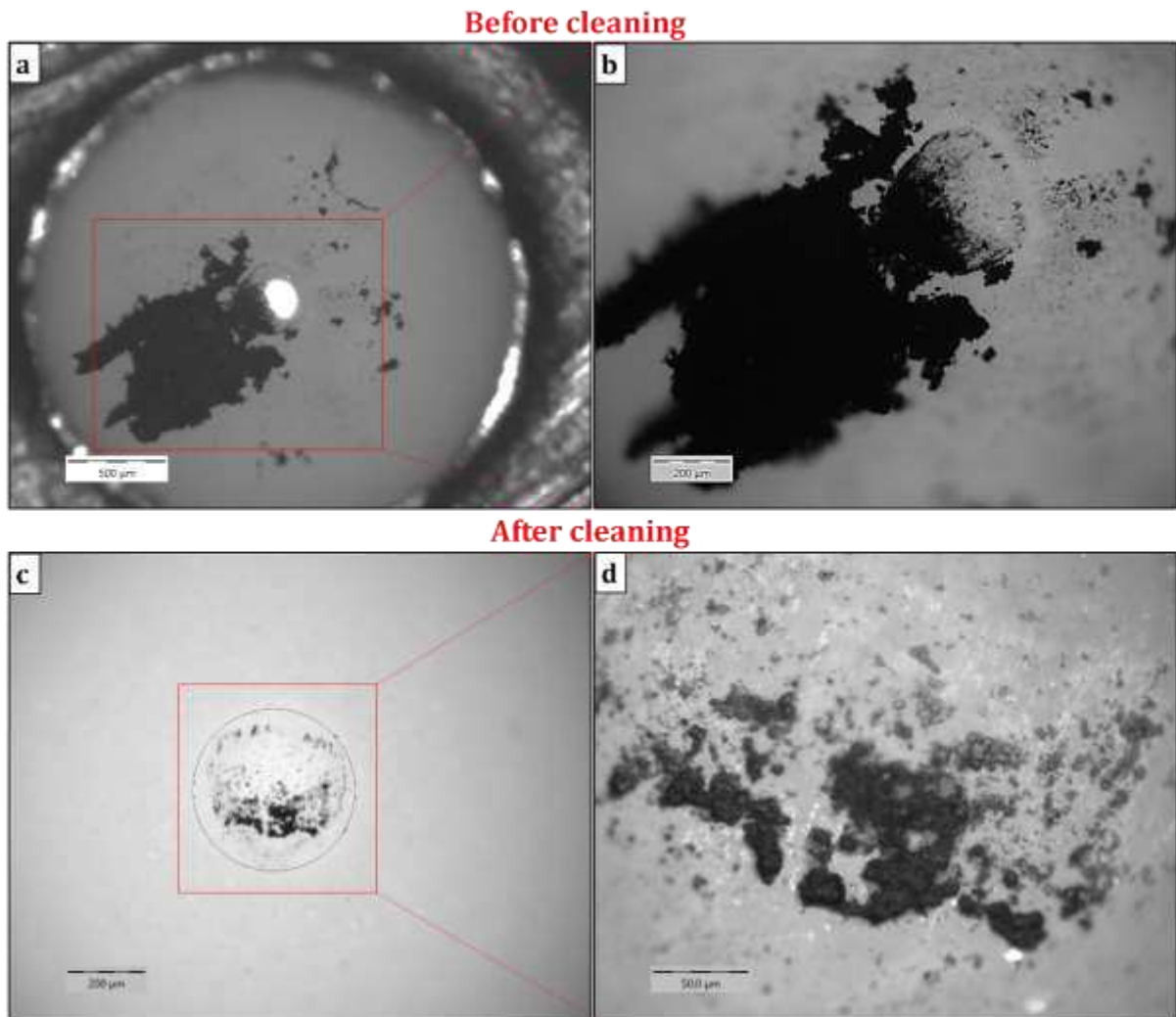


Fig. 19. Optical images of the Al_2O_3 ball after dry sliding friction test against Ti_3AlC_2 - Ti_2AlC MAX phase composite.

5. Wear mechanism

The wear mechanism appears to be dominated by a wear transition from deformation induced wear to oxidative controlled wear due to the evolution of triboreaction products, possibly owing to frictional heating. The wear mechanisms are further explained in the following sections:

4.1. Deformation induced wear

Plastic deformation at the sliding interface induced on the asperity contact scale as well as deformation induced basal plane slip [50] will lead to microfracture and subsequent generation of wear debris which acts as an abrasive third-body, leading to the observed sharp increase in CoF in the early stage during dry sliding friction (regime I). The deformation morphology shows that grain buckling, initiated possibly by basal plane slip, led to cracking because the

shear strains between the bent and the unbent layers are incompatible, thus leading to grain delamination in agreement with the deformation mechanism reported in MAX-phases [31]. It is apparent that basal slip induced grain buckling is the main deformation mechanism for this composite. As a result there are two damage modes i.e., delamination and grain fracture, both of which are induced by buckling. According to Yanchun et al. [50], owing to deformation by basal slip, dislocations will move throughout the entire grain and preferentially pileup at grain boundaries to bring about grain boundary cracking. In general, extensive micro-deformation mechanisms incorporating basal plane slipping, grain buckling, delamination, kink band formation and fracture of layers have been reported as operative deformation mechanisms in MAX-phases. Nonetheless, it should be highlighted that the presence of gaps in the matrix will expedite grain pull-out which might have also played a major role in the high COF observed in regime I.

4.2. *Tribo-oxidative wear*

According to the coefficient of friction plot, after a certain sliding distance (probably necessary for sufficient oxide film generation and compaction), a transition from a deformation induced wear mechanism to a different wear mechanism characterized by lower friction coefficient took place, thus highlighting the influence of tribofilm evolution. Raman and EELS analysis of the wear tracks and wear debris clearly indicates that after the transition, the wear mechanism changed from deformation-induced to tribo-oxidative wear mechanism. The reduction in friction coefficient was therefore due to the evolution of the lubricating action initiated by tribofilms. The evolution of tribo-oxidative wear mechanism was probably due to frictional heating owing to the increased contact temperature attained during sliding. It is believed that the fractured grains at the sliding surface due deformation induced wear as well as grain pull-outs were pulverized inside the wear track owing to repeated sliding, thus generating wear debris that subsequently becomes compacted as a function of time. The compacted wear debris is then oxidized due to frictional heating, to generate a protective easy-shearing tribofilm at the sliding surface, bringing about the wear transition from deformation induced to tribo-oxidative wear. Furthermore, it is believed that graphitic carbon was initially formed at the sliding surface prior to the evolution of rutile and titanium oxycarbide subsequently triggered by frictional heating.

5. **Conclusions**

Fully dense polycrystalline $\text{Ti}_3\text{AlC}_2\text{-Ti}_2\text{AlC}$ dual MAX-phase composite was successfully synthesized using spark plasma sintering (SPS). The microstructure and tribological properties of the as-synthesized sample was studied, and the following salient conclusions can be drawn:

(1) The resulting $\text{Ti}_3\text{AlC}_2\text{-Ti}_2\text{AlC}$ composite microstructure displayed a nano-laminated structure typical of laminated carbides with exaggerated grain growth of the phases observed and possibly linked to the holding time during the synthesis. Deformation induced by indentation showed micro-scale plasticity encompassing energy absorbing mechanisms such as grain buckling, delamination, kink-band formation, chevron fold, grain push-out and pull-out and eventual grain fracture.

(2) The lubrication and wear phenomena of the $\text{Ti}_3\text{AlC}_2\text{-Ti}_2\text{AlC}$ is fundamentally dependent on the tribo-oxidation transfer film formed at the sliding surface. Owing to the good oxidation resistance of these Al-containing MAX phases, tribo-oxidation is delayed. Once tribo-oxidative layer formation at the sliding surface is delayed, three-body abrasive wear that originates from the direct contact between the counterparts leading to pull-out of grains and subsequent fracture will dominate the wear mechanism.

(3) The wear rate of the composite was particularly high owing to low hardness and grain pull-outs. One way to improve the wear resistance is to consider appropriate interface combination and reinforcement with TiAl intermetallics which will enhance simultaneously both the composite hardness as well as fill the voids and/or gaps due to the plate-like grain structure and different grain sizes of the MAX phases in the matrix. The presence of intermetallic phase particles in the matrix might help deteriorate the oxidation resistance of the MAX phases, thus expediting the formation of transfer film via tribo-oxidation.

References

1. Barsoum, M.W., *MAX phases : properties of machinable ternary carbides and nitrides*. 2013: Weinheim, Germany : Wiley-VCH Verlag GmbH & Co. KGaA, 2013.
2. Barsoum, M.W., *The MN+1AXN phases: A new class of solids*. Progress in Solid State Chemistry, 2000. **28**(1): p. 201-281.
3. Hu, C., et al., *New phases' discovery in MAX family*. International Journal of Refractory Metals and Hard Materials, 2013. **36**: p. 300-312.
4. Kanoun, M.B., S. Goumri-Said, and K. Abdullah, *8 - Theoretical study of physical properties and oxygen incorporation effect in nanolaminated ternary carbides 211-MAX phases A2 - Low, I.M.*, in *Advances in Science and Technology of Mn+1axn Phases*. 2012, Woodhead Publishing. p. 177-196.
5. Barsoum, M.W. and M. Radovic, *Elastic and Mechanical Properties of the MAX Phases*, in *Annual Review of Materials Research, Vol 41*, D.R. Clarke and P. Fratzl, Editors. 2011, Annual Reviews: Palo Alto. p. 195-227.
6. Eklund, P., et al., *The Mn + 1AXn phases: Materials science and thin-film processing*. Thin Solid Films, 2010. **518**(8): p. 1851-1878.
7. Zhou, Y. and Z. Sun, *Electronic Structure and Bonding Properties Layered Machinable Ti2AlC and Ti2AlN*. Physical Review B, 2000. **61**: p. 75120-12573.
8. Córdoba, J.M., et al., *Synthesis of Ti3SiC2 Powders: Reaction Mechanism*. Journal of the American Ceramic Society, 2007. **90**(3): p. 825-830.
9. El-Raghy, T., et al., *Damage mechanisms around hardness indentations in Ti3SiC2*. Journal of the American Ceramic Society, 1997. **80**(2): p. 513-516.
10. Low, I.M., *Vickers contact damage of micro-layered Ti3SiC2*. Journal of the European Ceramic Society, 1998. **18**(6): p. 709-713.

11. Zhou, A., C.-a. Wang, and Y. Huang, *A possible mechanism on synthesis of Ti₃AlC₂*. Materials Science and Engineering: A, 2003. **352**(1): p. 333-339.
12. Peng, C., et al., *A novel simple method to stably synthesize Ti₃AlC₂ powder with high purity*. Materials Science and Engineering: A, 2006. **428**(1): p. 54-58.
13. Akhlaghi, M., et al., *Self-propagating high-temperature synthesis of Ti₃AlC₂ MAX phase from mechanically-activated Ti/Al/graphite powder mixture*. Ceramics International, 2018. **44**(8): p. 9671-9678.
14. Pietzka, M.A. and J.C. Schuster, *Phase equilibria of the quaternary system Ti-Al-Sn-N at 900 °C*. Journal of Alloys and Compounds, 1997. **247**(1): p. 198-201.
15. Chlubny, L., et al., *Processing and properties of MAX phases - based materials using SHS technique*. Arch. Metall. Mater., 2015. **60**(2): p. 859-863.
16. Ai, T., et al., *Microstructural and mechanical properties of dual Ti₃AlC₂-Ti₂AlC reinforced TiAl composites fabricated by reaction hot pressing*. Ceramics International, 2014. **40**(7, Part A): p. 9947-9953.
17. Barsoum, M.W., T. El-Raghy, and M. Ali, *Processing and characterization of Ti₂AlC, Ti₂AlN, and Ti₂AlC_{0.5}N_{0.5}*. Metallurgical and Materials Transactions A, 2000. **31**(7): p. 1857-1865.
18. Kulkarni, S.R. and A.V.D.K.-H. Wu, *Synthesis of Ti₂AlC by spark plasma sintering of TiAl-carbon nanotube powder mixture*. Journal of Alloys and Compounds, 2010. **490**(1): p. 155-159.
19. Wang, C., et al., *Irradiation-induced structural transitions in Ti₂AlC*. Acta Materialia, 2015. **98**: p. 197-205.
20. Zhou, W., et al., *Fabrication of high purity dense Ti₂AlC-Ti₃AlC₂ composite by spark plasma sintering method*. Journal of Materials Science, 2005. **40**(13): p. 3559-3560.
21. Furnish, T.A., et al., *The onset and evolution of fatigue-induced abnormal grain growth in nanocrystalline Ni-Fe*. Journal of Materials Science, 2017. **52**(1): p. 46-59.
22. SELSING, J., *Internal Stresses in Ceramics*. Journal of the American Ceramic Society, 1961. **44**(8): p. 419-419.
23. Lin, Z.J., et al., *Microstructural characterization of layered ternary Ti₂AlC*. Acta Materialia, 2006. **54**(4): p. 1009-1015.
24. Ai, T., et al., *Processing, microstructural characterization and mechanical properties of in situ Ti₃AlC₂/TiAl₃ composite by hot pressing*. Materials Science and Engineering: A, 2014. **610**: p. 297-300.
25. Rahaei, M.B., et al., *Manufacturing of high volume fraction of Ti₃AlC₂-Ti₂AlC metallic ceramics as nano-multilayered structures through high energy milling, hot pressing and liquid phase sintering*. Materials Characterization, 2017. **128**: p. 176-183.
26. Tzenov, N.V. and M.W. Barsoum, *Synthesis and Characterization of Ti₃AlC₂*. Journal of the American Ceramic Society, 2000. **83**(4): p. 825-832.
27. Milman, Y.V., et al., *Mechanical behaviour of Al₃Ti intermetallic and L12 phases on its basis*. Intermetallics, 2001. **9**(9): p. 839-845.
28. Wang, P., et al., *Synthesis of Ti₂AlC by hot pressing and its mechanical and electrical properties*. Transactions of Nonferrous Metals Society of China, 2007. **17**(5): p. 1001-1004.
29. Barsoum, M.W., L. Farber, and T. El-Raghy, *Dislocations, kink bands, and room-temperature plasticity of Ti₃SiC₂*. Metallurgical and Materials Transactions A, 1999. **30**(7): p. 1727-1738.
30. Li, S.B., L.F. Cheng, and L.T. Zhang, *Identification of damage tolerance of Ti₃SiC₂ by hardness indentations and single edge notched beam test*. Materials Science and Technology, 2002. **18**(2): p. 231-233.
31. Zhang, Z.F., et al., *Micron-scale Deformation and Damage Mechanisms of Ti₃SiC₂ Crystals Induced by Indentation*. Advanced Engineering Materials, 2004. **6**(12): p. 980-983.
32. Prikhna, T.A., et al., *Mechanical properties of materials based on MAX phases of the Ti-Al-C system*. Journal of Superhard Materials, 2012. **34**(2): p. 102-109.

33. Sun, Z., et al., *Ternary Compound Ti₃SiC₂: Part II. Deformation and Fracture Behavior at Different Temperatures*. Materials transactions, 2002. **43**(3): p. 432-435.
34. El-Raghy, T., et al., *Processing and Mechanical Properties of Ti₃SiC₂: II, Effect of Grain Size and Deformation Temperature*. Journal of the American Ceramic Society, 1999. **82**(10): p. 2855-2860.
35. Drouelle, E., et al., *Deformation mechanisms during high temperature tensile creep of Ti₃AlC₂ MAX phase*. Journal of Alloys and Compounds, 2017. **693**: p. 622-630.
36. Amini, S., M.W. Barsoum, and T. El-Raghy, *Synthesis and Mechanical Properties of Fully Dense Ti₂SC*. Journal of the American Ceramic Society, 2007. **90**(12): p. 3953-3958.
37. Blau, P.J., *Interpretations of the friction and wear break-in behavior of metals in sliding contact*. Wear, 1981. **71**(1): p. 29-43.
38. El-Raghy, T., P. Blau, and M.W. Barsoum, *Effect of grain size on friction and wear behavior of Ti₃SiC₂*. Wear, 2000. **238**(2): p. 125-130.
39. Presser, V., et al., *First-order Raman scattering of the MAX phases: Ti₂AlN, Ti₂AlC_{0.5}N_{0.5}, Ti₂AlC, (Ti_{0.5}V_{0.5})₂AlC, V₂AlC, Ti₃AlC₂, and Ti₃GeC₂*. Journal of Raman Spectroscopy, 2012. **43**(1): p. 168-172.
40. Jonathan E. Spanier, S.G., Maher S. Amer and Michel W. Barsoum, *Vibrational Behavior of the Mn+1AX_n Phases from First-Order Raman Scattering (M=Ti, V, Cr, A=Si, X=C, N)*. Physical Review B: Condensed Matter and Materials Physics, 2005. **71**(1 (2005)).
41. Frank, O., et al., *Raman spectra of titanium dioxide (anatase, rutile) with identified oxygen isotopes (16, 17, 18)*. Physical Chemistry Chemical Physics, 2012. **14**(42): p. 14567-14572.
42. Balachandran, U. and N.G. Eror, *Raman spectra of titanium dioxide*. Journal of Solid State Chemistry, 1982. **42**(3): p. 276-282.
43. Wu, C.-h., S.-y. Chen, and P. Shen, *CH doped anatase nanospheres with disordered shell and planar defects synthesized by pulsed laser ablation of bulk Ti in tetraethyl orthosilicate*. CrystEngComm, 2014. **16**(11): p. 2220-2229.
44. Tuinstra, F. and J.L. Koenig, *Raman Spectrum of Graphite*. The Journal of Chemical Physics, 1970. **53**(3): p. 1126-1130.
45. Pang, W.K., et al., *12 - Oxidation characteristics of Ti₃AlC₂, Ti₃SiC₂ and Ti₂AlC*, in *Advances in Science and Technology of Mn+1AX_n Phases*. 2012, Woodhead Publishing. p. 289-322.
46. Zhang, H.B. and K.G. Nickel, *Hydrothermal oxidation of Ti₃SiC₂*. 2012. 323-354.
47. Souchet, A., et al., *Tribological duality of Ti₃SiC₂*. Tribology Letters, 2005. **18**(3): p. 341-352.
48. Gupta, S. and M.W. Barsoum, *On the tribology of the MAX phases and their composites during dry sliding: A review*. Wear, 2011. **271**(9-10): p. 1878-1894.
49. Barsoum, M.W., et al., *Kinking Nonlinear Elastic Solids, Nanoindentations, and Geology*. Physical Review Letters, 2004. **92**(25): p. 255508.
50. Zhou, Y. and Z. Sun, *Micro-scale plastic deformation of polycrystalline Ti₃SiC₂ under room-temperature compression*. Journal of the European Ceramic Society, 2001. **21**(8): p. 1007-1011.